Research Square

Preprints are preliminary reports that have not undergone peer review.
They should not be considered conclusive, used to inform clinical practice,
or referenced by the media as validated information.

Near-Field Multiuser Multi-Beam Design for XL-RIS-Aided Systems Based on Wavenumber-Domain Projection

Dongqin Xing
Qinghai Minzu University
Guicai Yu
yuguicai@ncu.edu.cn

Qinghai Minzu University

Article

Keywords:

Posted Date: November 10th, 2026

DOI: https://doi.org/10.21203/rs.3.rs-11424209/v1

License: This work is licensed under a Creative Commons Attribution 4.0 International License.
Read Full License

Additional Declarations: No competing interests reported.

Near-Field Multiuser Multi-Beam Design for XL-RIS-Aided Systems Based on Wavenumber-Domain Projection

Dongqin Xing[1,2,3], Guicai Yu[1,2,3*]

1. School of Intelligent Science and Engineering, Qinghai Minzu University, Xining 810007, China;

2. National Experimental Teaching Demonstration Center for Communication Engineering, Qinghai Minzu University, Xining 810007, China;

3. Key Laboratory of Communication Engineering, Qinghai Minzu University, Xining 810007, China

*** Corresponding Author Name and E-Mail:** Guicai Yu (yuguicai@ncu.edu.cn)

Abstract: As the aperture of an extremely large-scale reconfigurable intelligent surface (XL-RIS) increases, its Rayleigh distance also increases, making near-field spherical-wave propagation increasingly important. Conventional far-field discrete Fourier transform (DFT) codebooks cannot accurately match the distance-dependent phase profiles of near-field channels, leading to angular-domain energy leakage and inaccurate beam focusing. To address this issue, this paper proposes a near-field multiuser multi-beam design based on wavenumber-domain (WD) projection for XL-RIS-aided systems. First, a continuous-aperture near-field channel model is established to characterize cascaded spherical-wave propagation along the base station (BS)–XL-RIS–user links. The XL-RIS reflection coefficients are represented by a continuous function subject to a constant-modulus constraint, consistent with the phase-only control of the passive XL-RIS. The cascaded channel function and the reflection coefficient function are then orthogonally projected onto a two-dimensional Fourier wavenumber basis to obtain a WD representation. A circular low-wavenumber truncation scheme is subsequently introduced to retain the dominant modes and yield a finite-dimensional representation, and an upper bound on the truncation error is derived. Based on this representation, the problem of maximizing the minimum user spectral efficiency under equal time-slot allocation is addressed using a fairness-oriented target-gain matching surrogate. The surrogate problem is solved using a block coordinate descent algorithm with majorization–minimization updates (BCD-MM). Simulation results show that the proposed method outperforms all considered benchmarks in terms of worst-user spectral efficiency and reliability. At a signal-to-noise ratio (SNR) of 0 dB, the proposed method improves the mean minimum user spectral efficiency by approximately 17.7% compared with the near-field codebook-based BCD-MM scheme, the best-performing benchmark for this metric. The truncated WD representation also retains the dominant wavenumber modes with limited projection distortion.

Keywords: Extremely large-scale reconfigurable intelligent surface (XL-RIS), Near field, Multi-beam; Wavenumber domain projection, Constant modulus constraint

1. Introduction

The rapid development of sixth-generation (6G) wireless systems has led to increasingly stringent requirements for ultra-high data rates, massive connectivity, ubiquitous coverage, and highly reliable transmission. To meet these requirements, future wireless networks are expected to exploit large electromagnetic (EM) apertures and programmable propagation environments, enabling more flexible control of signal transmission[1],[2]. Reconfigurable intelligent surfaces (RISs), which consist of numerous low-cost passive reflecting elements with programmable phase responses, have emerged as a promising technology for reshaping wireless propagation. By adjusting the phases of the reflected waves, RISs can provide additional spatial degrees of freedom and improve transmission performance without requiring active radio-frequency (RF) amplification[3].

To further enhance spatial control in RIS-aided systems, extremely large-scale reconfigurable intelligent surfaces (XL-RISs) with substantially enlarged EM apertures have been proposed. Compared with conventional RISs, XL-RISs comprise many more reflecting elements and offer higher aperture gains, enabling finer spatial control and more flexible beam manipulation [4]. However, the enlarged apertures also increase the corresponding Rayleigh distances, making near-field (NF) operation increasingly important. As discussed in [4], XL-RIS and extremely large-scale multiple-input multiple-output (XL-MIMO) systems are expected to operate more frequently in the radiative NF region, where conventional far-field (FF) assumptions become inadequate. Whereas FF

propagation can be approximated using planar waves, NF propagation exhibits spherical-wave characteristics, with the EM response depending jointly on the propagation direction and distance [5]. Accurate channel characterization and beam design for XL-RIS systems therefore require consideration of distance-dependent phase variations in addition to angular information.

These propagation characteristics introduce additional challenges for multiuser transmission, as a single passive XL-RIS reflection profile must accommodate the beam-focusing requirements of users at different spatial locations. Developing an efficient channel representation and optimization framework for NF XL-RIS-aided multiuser transmission thus remains an important research problem.

Prior Works

RISs have recently attracted significant attention as an enabling technology for next-generation wireless communications due to their ability to manipulate EM propagation through programmable phase control. With growing interest in XL-RISs, NF beam focusing and multiuser transmission have become important research directions. Considerable research effort has therefore been devoted to NF beam training, codebook design, and beamforming optimization for large-aperture RIS systems. These studies mainly aim to address the challenges of beam acquisition and beam focusing introduced by the additional distance dimension in NF propagation. Compared with conventional FF RIS beamforming designs, NF designs need to jointly exploit angular and distance information, motivating the development of distance-aware codebooks, location-assisted beamforming strategies, and optimization-based multi-beam transmission frameworks.

For NF MIMO and XL-RIS systems, codebook-based approaches have been extensively studied due to their relatively low implementation complexity. Distance-aware codebooks and joint angle–distance codebooks were developed alongside beam training strategies to improve beam acquisition efficiency [6]. A low-overhead beam training scheme was also proposed for NF XL-RIS systems in [7]. Under practical discrete phase-shift constraints, multi-resolution codebook design and multiuser interference management were investigated in [8]. Beyond codebook-based approaches, optimization-based multi-beam transmission schemes have received increasing attention because they directly optimize the reflection coefficients under hardware constraints. In [9], an NF XL-RIS multi-beam design method was proposed based on auxiliary phase variables associated with the desired beam gains, with the resulting constant-modulus optimization problem solved using the BCD-MM algorithm. Location-driven beamforming was also investigated in [10], while NF transmission aided by simultaneously transmitting and reflecting reconfigurable intelligent surfaces (STAR-RISs) was studied in [11]. Moreover, NF and hybrid-field channel estimation problems were explored in [12],[13]. Wideband RIS-aided NF beamforming and beamforming for large intelligent surfaces were investigated in [14] and [15], respectively. However, existing codebook-based methods generally rely on predefined spatial grids, which can lead to quantization errors and off-grid mismatches when representing continuous NF channels.

To address the limitations of spatial-grid-based representations, wavenumber-domain (WD) methods provide a physically grounded framework for characterizing EM propagation over electrically large apertures. By representing EM fields using orthogonal spatial-frequency modes, WD approaches offer a unified description of NF and FF propagation, extending conventional angular-domain representations. In NF multiuser communications, the additional distance dimension has been exploited for user separation and beam focusing [16],[17],[18]. Beamforming optimization frameworks have also been investigated for holographic XL-MIMO systems [19].

For continuous EM surfaces, Fourier plane-wave series expansions were developed to represent holographic

MIMO channels in the wavenumber domain [20]. A unified WD framework for FF and NF propagation was established in [21], revealing the limitations of conventional DFT-based angular representations. The sparsity and orthogonality of wavenumber modes were also exploited for channel estimation and signal processing in [22],[23]. For multiuser continuous-aperture transmission, a pattern-division multiplexing (PDM) scheme was developed to project continuous current patterns onto a finite set of orthogonal Fourier basis functions and optimize the corresponding projection coefficients [24]. A two-timescale beamforming optimization framework for holographic MIMO surfaces was also investigated in [25]. More recently, the continuous-aperture array (CAPA) concept has been proposed as a general framework for directly controlling EM source distributions over electrically large apertures [26]. Existing studies have investigated capacity characterization [27], beamforming optimization [28], multiuser transmission [29], diversity and multiplexing [30], and integrated sensing and communication [31] for CAPA systems. These studies highlight the potential of WD and continuous-aperture representations for exploiting large EM apertures in future communication systems. Extending these approaches to passive XL-RIS systems requires accounting for the constant-modulus constraint on the reflection profile, which couples the corresponding WD coefficients.

Motivation

Although significant progress has been made in NF XL-RIS beam design, an efficient representation framework that both captures the physical characteristics of spherical-wave propagation and accommodates practical passive reflection constraints remains lacking. As summarized in Table 1, existing studies can generally be classified into three categories: codebook-based approaches, element-domain optimization approaches, and continuous-aperture EM design approaches. Codebook-based methods reduce beam-search complexity but usually rely on predefined spatial grids, which may introduce quantization errors and off-grid mismatches when representing continuous NF channels. Element-domain optimization methods can directly handle the constant-modulus constraint of passive XL-RISs, but they generally lack an explicit EM representation of the continuous aperture. Continuous-aperture and holographic approaches provide explicit EM descriptions, but most focus on actively controlled source distributions over continuous apertures rather than phase-only reflection control in passive XL-RISs.

WD representation provides a physically meaningful framework for describing EM propagation over electrically large apertures by decomposing fields into orthogonal spatial-frequency modes. However, existing WD-based frameworks mainly focus on holographic MIMO, CAPA systems, or active EM surfaces, in which the corresponding source or current distributions can be directly optimized. In contrast, passive XL-RIS systems employ a shared reflection profile whose WD coefficients are coupled by the constant-modulus constraint, resulting in a fundamentally different optimization structure. Therefore, these WD frameworks cannot be directly applied to passive XL-RIS-aided multiuser transmission without modification.

These observations call for a WD design framework that captures the spatial structure of continuous-aperture NF channels while accommodating the phase-only control constraints of passive XL-RIS elements. Accordingly, a WD projection-based multiuser multi-beam approach is developed for XL-RIS-aided systems. Dominant wavenumber modes are retained through low-wavenumber truncation to reduce the representation dimension. The shared reflection coefficient vector is jointly optimized for all users under the constant-modulus constraint to improve the minimum user spectral efficiency. The proposed design is evaluated in terms of worst-user spectral efficiency, statistical reliability, and computational cost.

Table 1. Comparison of near-field XL-RIS beamforming works

Reference	System Model	RIS Type	Propagation Model	Design Method	Representation Domain	Remarks
[6]	NF RIS-MIMO	Passive RIS	NF spherical-wave channel	Angle-distance codebook	Codebook domain	Beam training
[7]	NF XL-RIS training	Passive XL-RIS	NF channel	Low-overhead beam training	Codebook domain	Training overhead reduction
[8]	Discrete NF XL-RIS MIMO	Passive XL-RIS	NF channel	Multi-resolution codebook and interference management	Codebook domain	Phase quantization consideration
[9]	NF XL-RIS multi-beam	Passive XL-RIS	Spherical-wave channel	BCD-MM optimization	Element domain	Constant-modulus optimization
[10]	Location-driven NF RIS	Passive RIS	Location-dependent NF	Location-driven beamforming	Element domain	Location information exploitation
[12]	NF XL-RIS channel estimation	XL-RIS-assisted MIMO	NF channel	Hybrid beamforming channel estimation	Channel domain	CSI acquisition
[14]	Wideband NF RIS	Passive RIS	Wideband NF	Wideband beamforming	Element domain	Wideband transmission
[19]	Holographic XL-MIMO multi-user	Holographic MIMO surface	NF model	Multi-user beamforming	Continuous aperture	Continuous surface control
[20]	Holographic MIMO	Continuous aperture surface	EM field	Fourier expansion	Wavenumber domain	WD channel representation
[21]	Unified holographic MIMO	Continuous aperture surface	Unified NF/FF	WD framework	Wavenumber domain	DFT limitation analysis
[24]	Multi-user continuous-aperture MIMO	Continuous-aperture MIMO	Continuous EM	PDM	Fourier basis	Multi-user transmission
[26]	CAPA framework	CAPA	EM aperture	Source distribution control	Continuous aperture	Large-aperture framework
[28]	CAPA beamforming	CAPA	Continuous EM	CAPA beamforming optimization	Continuous aperture	Continuous beamforming
[29]	Multi-user CAPA systems	CAPA	Continuous EM	Optimal multi-user beamforming	Continuous aperture	Multi-user transmission
This Work	NF XL-RIS multiuser multi-beam	Passive XL-RIS	Continuous spherical-wave channel	WD-based multiuser beam design	Wavenumber domain	Passive constant-modulus multi-beam optimization

Contributions

The main contributions of this work to near-field XL-RIS-aided multi-user communication systems are summarized as follows:

- A continuous-aperture NF channel representation framework is developed for passive XL-RIS multi-beam design. Specifically, spherical-wave propagation along the cascaded BS–XL-RIS–user links is modeled using the scalar Green's function, and both the cascaded channel function and the XL-RIS reflection profile are orthogonally projected onto a two-dimensional Fourier wavenumber basis. This formulation provides a finite-dimensional representation of continuous EM propagation suitable for multi-beam optimization while preserving the physical characteristics of NF channels.
- A WD multiuser multi-beam design framework is proposed for passive XL-RIS systems under the constant-modulus constraint. Unlike conventional angular-domain DFT codebook-based methods and element-domain optimization approaches, the proposed framework exploits the orthogonality and spatial-frequency structure of WD modes to represent distance-dependent NF propagation, enabling efficient multiuser beamforming with a shared passive reflection profile.
- A circular low-wavenumber truncation strategy is developed to reduce the representation dimension, and the truncation error is theoretically characterized. By retaining the dominant low-wavenumber modes, the proposed method reduces the infinite-dimensional continuous-aperture representation to a compact finite-dimensional model.

An explicit upper bound on the truncation-induced deviation in effective channel gain is also derived, providing a theoretical basis for assessing the trade-off between representation accuracy and computational complexity.

- A fairness-oriented optimization framework is developed to maximize the minimum user spectral efficiency under equal time-slot allocation. The resulting nonconvex constant-modulus optimization problem is addressed through a target-gain matching surrogate problem, which is solved using a block coordinate descent algorithm with majorization–minimization updates (BCD-MM). The proposed WD representation facilitates efficient multiuser multi-beam optimization.
- Extensive numerical evaluations are conducted using a spherical-wave NF channel model to validate the effectiveness of the proposed method. The proposed WD design outperforms the NF codebook-based BCD-MM, NF single-beam, FF single-beam, and random-phase benchmarks in terms of worst-user spectral efficiency and reliability across a range of SNRs, numbers of users, XL-RIS aperture sizes, and truncation radii. The simulation results also demonstrate that the proposed truncation strategy retains the dominant channel energy with limited projection distortion.

2. Model and Problem Formulation

An NF XL-RIS-aided multiuser downlink communication model is established, and a reflection-phase optimization problem is formulated for multiuser multi-beam focusing under the constant-modulus constraint of the passive XL-RIS. The cascaded BS–XL-RIS–user links are represented by equivalent channel gains, and the shared reflection coefficient vector serves as the sole design variable. The Rayleigh distance and the propagation distances of the BS–XL-RIS and XL-RIS–user links are used to characterize NF operation. A continuous-aperture cascaded channel model based on spherical-wave propagation is then developed to explain the mismatch between angular-domain DFT codewords and NF channels. Finally, the constant-modulus constraint and the effective channel gains for all users are specified. A spectral efficiency model under equal time-slot allocation is then established, and the problem of maximizing the minimum user spectral efficiency is explicitly formulated.

2.1 Signal Model

Consider an XL-RIS-aided multiuser downlink system in which a BS equipped with M antennas serves K single-antenna users through an XL-RIS comprising N passive reflecting elements. The XL-RIS consists of N_1 rows and N_2 columns, with $N = N_1 N_2$, and lies in the y0z-plane with its center at the origin. The user set is denoted by $\mathrm{K} = \{1,\ldots,K\}$. In the deployment scenario considered, the XL-RIS is mounted on a high wall or tower with few surrounding scatterers. The direct BS–user links are assumed to be blocked, and communication takes place via reflection from the XL-RIS. A narrowband quasi-static channel model is adopted, and the XL-RIS elements are assumed to support continuously adjustable phase shifts. Accordingly, the received signal at user k is expressed as

$$y_k = \boldsymbol{h}_{\mathrm{r},k}^{\mathrm{T}} \boldsymbol{\Theta} \boldsymbol{G} \boldsymbol{x} + n_k, \tag{1}$$

where y_k denotes the received signal at user k, $\boldsymbol{G} \in \mathbb{C}^{N \times M}$ denotes the BS–XL-RIS channel matrix, $\boldsymbol{h}_{\mathrm{r},k}^{\mathrm{T}} \in \mathbb{C}^{1 \times N}$ denotes the channel vector from the XL-RIS to user k, $\boldsymbol{x} \in \mathbb{C}^{M \times 1}$ denotes the precoded transmit signal vector at the BS, and n_k denotes additive white Gaussian noise (AWGN) with noise power σ^2. The diagonal reflection matrix of the XL-RIS is defined as $\boldsymbol{\Theta} = \mathrm{diag}(\boldsymbol{q})$, where $\boldsymbol{q} = [q_1,\ldots,q_N]^{\mathrm{T}}$ denotes the reflection coefficient vector

and q_n denotes the reflection coefficient of the n-th XL-RIS element.

Since the BS and the XL-RIS are at fixed locations and the BS–XL-RIS link is dominated by line-of-sight (LoS) propagation with limited scattering, the BS beam can be configured in advance to point toward the XL-RIS. Following [9], the BS beamforming vector is therefore held fixed, allowing the BS to be modeled as an effective single-antenna transmitter. The BS–XL-RIS link and the link from the XL-RIS to user k are then combined into an effective cascaded channel for user k. Accordingly, the received signal at user k can be rewritten as

$$y_k = \sqrt{P_k}\left(\boldsymbol{q}^{\mathrm{T}}\bar{\boldsymbol{h}}_k\right)x_k + n_k, \tag{2}$$

where P_k denotes the transmit power allocated to user k, x_k denotes the normalized data symbol intended for user k and satisfies $\mathrm{E}\left\{|x_k|^2\right\}=1$, and $\bar{\boldsymbol{h}}_k$ denotes the effective cascaded channel vector for user k, obtained by combining the BS–XL-RIS link and the link from the XL-RIS to user k. Equation (2) expresses the end-to-end channel for user (k) in terms of a scalar effective channel gain, with the XL-RIS reflection coefficient vector $\boldsymbol{q}$ as the design variable. The vector $\boldsymbol{q}$ is shared by all users and is subject to the constant-modulus constraint, which reflects the phase-only control of the passive XL-RIS elements. The central problem addressed in this paper is therefore to design $\boldsymbol{q}$ to provide sufficiently large effective channel gains for all K users.

2.2 Near-Field Cascaded Channel Model

As the XL-RIS aperture increases, its NF region expands. To determine whether the BS and the users lie within this region, the Rayleigh distance is used as the conventional boundary between the NF and FF regions. The Rayleigh distance of the XL-RIS is defined as

$$R_{\mathrm{Ray}} = \frac{2D^2}{\lambda}, \tag{3}$$

where $D=\sqrt{L_y^2+L_z^2}$ denotes the diagonal length of the XL-RIS aperture, L_y and L_z denote its physical lengths along the y- and z-axes, respectively, and λ denotes the carrier wavelength. For a fixed carrier wavelength, the Rayleigh distance R_{Ray} increases quadratically with D. For an XL-RIS with a large aperture, R_{Ray} can reach tens of meters, making the BS and the users more likely to lie within the NF region. Since the cascaded link through the XL-RIS comprises the BS–XL-RIS link and the link from the XL-RIS to user k, characterizing NF propagation along the cascaded link requires consideration of both propagation distances. Accordingly, the NF criterion for the cascaded link is expressed as

$$\frac{r_{\mathrm{RA}}r_{\mathrm{RD},k}}{r_{\mathrm{RA}}+r_{\mathrm{RD},k}} < R_{\mathrm{Ray}}, \tag{4}$$

where r_{RA} denotes the distance between the BS and the center of the XL-RIS, and $r_{\mathrm{RD},k}$ denotes the distance between user k and the center of the XL-RIS. When the criterion in Eq. (4) is satisfied, the cascaded channel is modeled using spherical-wave propagation. This criterion accounts for both propagation distances.

Under FF conditions, the propagation direction between the XL-RIS aperture and a given node can be approximated as constant across the aperture, allowing the corresponding channel to be characterized primarily by angular parameters. For a large-aperture XL-RIS operating in the NF region, however, the propagation distance to the BS or a user varies with position across the aperture. For a large-aperture XL-RIS operating in the NF region,

however, the propagation distance to the BS or a user varies with position across the aperture. The resulting phase profile cannot generally be represented accurately using a plane-wave approximation. Therefore, the cascaded BS–XL-RIS–user channel is modeled using spherical-wave propagation, with its response expressed as a function of position across the XL-RIS aperture. Let $\mathrm{S_R}=\left\{\boldsymbol{s}=(\boldsymbol{s}_x,\boldsymbol{s}_y,\boldsymbol{s}_z)\,|\,\boldsymbol{s}_x=0,|\boldsymbol{s}_y|\le \boldsymbol{L}_y/2,|\boldsymbol{s}_z|\le \boldsymbol{L}_z/2\right\}$ denote the continuous aperture of the XL-RIS and $\boldsymbol{s}\in\mathrm{S_R}$ denote the position vector of an arbitrary point on the aperture.

Let $\boldsymbol{r}_{\mathrm{B}}$ and $\boldsymbol{r}_k$ denote the position vectors of the BS and user k, respectively. For an aperture point with position vector $\boldsymbol{s}\in\mathrm{S_R}$, the distance to the BS is expressed as

$$d_{\mathrm{B}}(\boldsymbol{s})=\left\|\boldsymbol{s}-\boldsymbol{r}_{\mathrm{B}}\right\|_2. \tag{5}$$

Similarly, the distance from the aperture point $\boldsymbol{s}$ to user k is expressed as

$$d_k(\boldsymbol{s})=\left\|\boldsymbol{s}-\boldsymbol{r}_k\right\|_2. \tag{6}$$

Under the assumptions of single polarization and free-space LoS propagation, the propagation response between two spatial points is modeled using the following scalar Green's function:

$$G(\boldsymbol{s},\boldsymbol{r})=\frac{1}{4\pi\left\|\boldsymbol{s}-\boldsymbol{r}\right\|_2}\exp\left(-\mathrm{j}\kappa_0\left\|\boldsymbol{s}-\boldsymbol{r}\right\|_2\right), \tag{7}$$

where $G(\boldsymbol{s},\boldsymbol{r})$ denotes the free-space propagation response between points $\boldsymbol{s}$ and $\boldsymbol{r}$, $\kappa_0=2\pi/\lambda$ denotes the free-space wavenumber, and j denotes the imaginary unit. The factor $1/4\pi\left\|\boldsymbol{s}-\boldsymbol{r}\right\|_2$ describes the amplitude decay due to spherical spreading, while the exponential term describes the phase accumulated over the propagation distance. The continuous-aperture cascaded NF channel function is obtained by multiplying the propagation responses of the BS–XL-RIS link and the link from the XL-RIS to user k, with all factors independent of $\boldsymbol{s}$ absorbed into $\bar{\alpha}_k$. The resulting function is expressed as

$$\bar{h}_k(\boldsymbol{s})=\bar{\alpha}_k\frac{\exp\left(-\mathrm{j}\kappa_0\left(d_{\mathrm{B}}(\boldsymbol{s})+d_k(\boldsymbol{s})\right)\right)}{d_{\mathrm{B}}(\boldsymbol{s})d_k(\boldsymbol{s})}, \tag{8}$$

where $\bar{h}_k(\boldsymbol{s})$ denotes the cascaded NF channel response at aperture point $\boldsymbol{s}$ for user k, and $\bar{\alpha}_k$ collects the channel coefficients and normalization factors that are independent of $\boldsymbol{s}$. Unlike a model based on the FF plane-wave approximation, this model retains the nonlinear dependence of the total propagation distance $d_{\mathrm{B}}(\boldsymbol{s})+d_k(\boldsymbol{s})$ on the aperture position. The resulting phase profile depends on both the propagation directions and the distances to the BS and the user. Consequently, conventional angle-only DFT codewords generally cannot match this distance-dependent phase profile, leading to angular-domain energy leakage and beam-focusing errors. For an XL-RIS comprising N reflecting elements centered at $\{\boldsymbol{s}_n\}_{n=1}^{N}$ with inter-element spacing $d_{\mathrm{R}}=\lambda/2$, the sampled cascaded channel vector is $\bar{\boldsymbol{h}}_k=A_{\mathrm{e}}\left[\bar{h}_k(\boldsymbol{s}_1),\ldots,\bar{h}_k(\boldsymbol{s}_N)\right]^{\mathrm{T}}$, where A_{e} denotes the area of each XL-RIS element.

2.3. Constant-Modulus Reflection and User Effective Gain

An XL-RIS comprises numerous passive reflecting elements that lack RF amplification capability and therefore cannot actively amplify the incident signal. Under the ideal phase-only reflection model adopted here, the magnitude of each element's reflection coefficient is normalized to unity, while its phase is adjustable. Accordingly,

the reflection coefficient of the n-th XL-RIS element is expressed as $q_n = \exp(\mathrm{j}\phi_n)$, where $\phi_n \in [0, 2\pi)$ denotes the controllable phase shift of that element. The reflection coefficients therefore satisfy the following constant-modulus constraint:

$$|q_n| = 1, \forall n \in \{1, \ldots, N\}, \tag{9}$$

The effective channel gain for user k is obtained by coherently combining the reflected contributions across the XL-RIS aperture. In the continuous-aperture model, this gain is expressed as

$$g_k = \int_{S_R} \bar{\boldsymbol{h}}_k(\boldsymbol{s}) q(\boldsymbol{s}) \mathrm{d}\boldsymbol{s}, \tag{10}$$

where $q(\boldsymbol{s}) = \exp(\mathrm{j}\phi(\boldsymbol{s}))$, with $\phi(\boldsymbol{s})$ denoting the controllable phase shift at aperture point $\boldsymbol{s}$. After discretizing the continuous XL-RIS aperture into N reflecting elements, the reflection coefficient of the n-th element is $q_n = q(\boldsymbol{s}_n)$. The effective channel gain for user k can then be expressed as

$$g_k = \boldsymbol{q}^{\mathrm{T}} \bar{\boldsymbol{h}}_k, \tag{11}$$

where g_k is jointly determined by the shared reflection coefficient vector $\boldsymbol{q}$ and the cascaded channel vector $\bar{\boldsymbol{h}}_k$. Directly superimposing independently designed single-user codewords generally results in entries of $\boldsymbol{q}$ with magnitudes other than unity, thereby violating the constant-modulus constraint. Such superposition may also impair beam focusing and reduce the minimum effective channel gain across users. Therefore, $\boldsymbol{q}$ is jointly optimized for all users under the constant-modulus constraint.

2.4. Time-Division Access with a Shared Reflection Coefficient Vector

To account for the XL-RIS reconfiguration delay and control overhead, the reflection coefficient vector $\boldsymbol{q}$ is assumed to remain fixed throughout each channel coherence interval. Within each interval, the K NF users are served sequentially in K consecutive time slots of equal duration. Since the same vector is used in all time slots, it must be designed to provide effective beam focusing for all K users. Based on Eq. (2), the received SNR at user k in the k-th time slot can be expressed as

$$\gamma_k = \frac{P_k |g_k|^2}{\sigma^2}, \tag{12}$$

where $|g_k|^2$ denotes the effective channel power gain for user k. Under equal time-slot allocation, the spectral efficiency of user k can be expressed as

$$R_k = \frac{1}{K} \log_2(1 + \gamma_k) \tag{13}$$

where the factor $1/K$ accounts for the equal time-slot allocation among the K users within each channel coherence interval. Since all users share the same reflection coefficient vector $\boldsymbol{q}$, the minimum user spectral efficiency is adopted as the system performance metric to promote fairness among users. This metric is expressed as

$$R_{\min} = \min_{k \in \mathrm{K}} R_k, \tag{14}$$

where $R_{\min}$ denotes the minimum spectral efficiency among all users.

2.5. Problem Formulation

Under time-division access, the XL-RIS serves all near-field users within each channel coherence interval. The effective reflection gains across users are inherently coupled because of the limited spatial degrees of freedom at the XL-RIS. Maximizing the sum spectral efficiency may disproportionately benefit users with favorable channel conditions. This may degrade the performance of users with weaker channels and compromise user fairness. Therefore, the multi-beam design aims to maximize the minimum spectral efficiency among all users. Subject to the constant-modulus constraint imposed by the passive XL-RIS elements, the resulting optimization problem can be compactly expressed as

$$\begin{aligned} \mathrm{P}_0: \max_{\boldsymbol{q}} \min_{k\in\mathrm{K}} \frac{1}{K}\log_2\left(1+\frac{P_k\left|g_k\right|^2}{\sigma^2}\right), \\ \text{s.t.}\left|q_n\right|=1, \forall n\in\left\{1,\ldots,N\right\} \end{aligned} \tag{15}$$

where the objective is to maximize the minimum user spectral efficiency under time-division access, with all users sharing the same XL-RIS reflection coefficient vector $\boldsymbol{q}$. The constant-modulus constraint reflects the phase-only control of the passive XL-RIS elements. The resulting max–min optimization problem P_0 is nonconvex and challenging to solve. To make the multiuser design tractable, WD projection is used to obtain a compact representation of the cascaded NF channels, and a fairness-oriented target-gain matching surrogate problem is introduced below.

2.6. Target-Gain Matching Transformation

Since spectral efficiency is a monotonically increasing function of SNR and all users are allocated equal time slots and the same fixed transmit power, maximizing the minimum user spectral efficiency is equivalent to maximizing the minimum effective channel gain magnitude across users under the constant-modulus constraint. Moreover, the spectral efficiency of user k depends only on the magnitude of $\left|g_k\right|$ and is independent of its phase. Accordingly, a target gain magnitude can be specified for each user. Let $\boldsymbol{g}_0=\left[g_{0,1},\ldots,g_{0,K}\right]^{\mathrm{T}}$ denote the target gain magnitude vector, where $g_{0,k}>0$ specifies the desired effective channel gain magnitude for user (k). The equal-gain setting $g_{0,k}=g_0$ for all $k\in\mathrm{K}$ assigns the same target gain magnitude to all users, thereby promoting fairness. Furthermore, let $\boldsymbol{\zeta}=\left[\exp\left(\mathrm{j}\zeta_1\right),\ldots,\exp\left(\mathrm{j}\zeta_K\right)\right]^{\mathrm{T}}$ denote the auxiliary phase-factor vector, where $\left|\zeta_k\right|=1$ for all $k\in\mathrm{K}$. The resulting complex target-gain vector is expressed as

$$\bar{\boldsymbol{g}}=\boldsymbol{g}_0 \odot \boldsymbol{\zeta}. \tag{16}$$

This construction preserves the prescribed target gain magnitudes while allowing a separate target phase to be adjusted for each user. Accordingly, the resulting fairness-oriented target-gain matching surrogate problem can be expressed as

$$\begin{aligned} \mathrm{P}_1: \min_{\boldsymbol{q},\boldsymbol{\zeta}} \left\|\bar{\boldsymbol{g}}-\boldsymbol{g}(\boldsymbol{q})\right\|_2^2, \\ \text{s.t.}\left|q_n\right|=1, \left|\zeta_k\right|=1 \end{aligned} \tag{17}$$

where $\boldsymbol{g}\left(\boldsymbol{q}\right)=\left[\boldsymbol{q}^{\mathrm{T}}\bar{\boldsymbol{h}}_1,\ldots,\boldsymbol{q}^{\mathrm{T}}\bar{\boldsymbol{h}}_K\right]$ denotes the vector of effective channel gains for all users. Problem P_1 jointly optimizes the shared reflection coefficient vector $\boldsymbol{q}$ and the auxiliary phase-factor vector $\boldsymbol{\zeta}$ to match the

effective channel gains to their prescribed targets. This surrogate problem promotes balanced effective channel gain magnitudes across users and is intended to improve worst-user performance. A related target-gain matching strategy was adopted in [9] for NF constant-modulus multi-beam design. However, the effective channel gains represented by $\boldsymbol{g}(\boldsymbol{q})$ still arise from the coherent superposition of NF spherical waves over the continuous aperture. Therefore, a compact representation of the cascaded NF channels is required to enable efficient constant-modulus optimization.

3. Wavenumber-Domain Equivalent Representation

To obtain this compact representation while retaining the constant-modulus constraint, the cascaded NF channel function and the reflection coefficient function in the continuous-aperture integral are orthogonally projected onto a two-dimensional Fourier wavenumber basis. A low-wavenumber truncation criterion is then introduced to obtain a finite-dimensional representation, and the resulting energy retention ratio is evaluated. This procedure yields an explicit equivalent design matrix that linearly maps the spatial-domain reflection coefficient vector to the vector of effective channel gains for all users. Since the constant-modulus constraint is imposed in the spatial domain rather than in the WD, the spatial-domain reflection coefficient vector remains the optimization variable, whereas the WD coefficients are used only to construct the equivalent design matrix.

3.1. Wavenumber-Domain Basis and Channel Projection

To obtain a finite-dimensional WD representation of a spatial function over the continuous aperture, a two-dimensional orthogonal Fourier basis defined on $\mathrm{S_R}$ is adopted, and the resulting expansion is truncated. Let $\boldsymbol{m}=(m_1,m_2)\in\mathbb{Z}^2$ denote the two-dimensional WD index. The corresponding Fourier basis function is defined as

$$\Psi_{\boldsymbol{m}}(\boldsymbol{s})=\frac{1}{\sqrt{A_{\mathrm{R}}}}\exp\left[\mathrm{j}2\pi\left(\frac{m_1 s_y}{L_y}+\frac{m_2 s_z}{L_z}\right)\right], \tag{18}$$

where $\Psi_{\boldsymbol{m}}(\boldsymbol{s})$ denotes the two-dimensional Fourier basis function indexed by $\boldsymbol{m}$, m_1 and m_2 denote the integer mode indices along the y- and z-axes, respectively, and $A_{\mathrm{R}}=L_y L_z$ denotes the XL-RIS aperture area. It follows from Eq. (18) that the basis functions satisfy the conjugate-symmetry relation $\Psi_{-\boldsymbol{m}}(\boldsymbol{s})=\Psi_{\boldsymbol{m}}^{*}(\boldsymbol{s})$. They also satisfy the following orthonormality condition:

$$\int_{\mathrm{S_R}}\Psi_{\boldsymbol{m}}(\boldsymbol{s})\Psi_{\boldsymbol{n}}^{*}(\boldsymbol{s})\mathrm{d}\boldsymbol{s}=\delta_{\boldsymbol{m},\boldsymbol{n}}, \tag{19}$$

where $\boldsymbol{n}=(n_1,n_2)\in\mathbb{Z}^2$ denotes another two-dimensional WD index, and $\delta_{\boldsymbol{m},\boldsymbol{n}}$ denotes the Kronecker delta, which equals one if $\boldsymbol{m}=\boldsymbol{n}$ and zero otherwise. This relation confirms the orthonormality of the Fourier wavenumber basis functions, which are used to expand the cascaded NF channel function and the reflection coefficient function.

Since the reflection coefficient function $q(\boldsymbol{s})$ is square-integrable over the finite aperture $\mathrm{S_R}$, it can be expanded in terms of the above orthonormal basis as

$$q(\boldsymbol{s})=\sum_{\boldsymbol{m}}w_{\boldsymbol{m}}\Psi_{\boldsymbol{m}}(\boldsymbol{s}), \tag{20}$$

where $w_{\boldsymbol{m}}$ denotes the expansion coefficient of the reflection coefficient function associated with the wavenumber mode indexed by $\boldsymbol{m}$. The coefficient corresponding to the mode indexed by $\boldsymbol{n}$ is obtained by orthogonally

projecting $q(\boldsymbol{s})$ onto the associated basis function as follows:

$$w_{\boldsymbol{m}} = \int_{S_R} q(\boldsymbol{s}) \Psi_{\boldsymbol{m}}^{*}(\boldsymbol{s}) \mathrm{d}\boldsymbol{s}. \tag{21}$$

Similarly, for user k, the WD projection coefficient of the cascaded NF channel function corresponding to the wavenumber mode indexed by $\boldsymbol{m}$ is defined as

$$\tilde{h}_{k,\boldsymbol{m}} = \int_{S_R} \bar{h}_k(\boldsymbol{s}) \Psi_{\boldsymbol{m}}(\boldsymbol{s}) \mathrm{d}\boldsymbol{s}, \tag{22}$$

where $\tilde{h}_{k,\boldsymbol{m}}$ denotes the corresponding channel projection coefficient. The basis function $\Psi_{\boldsymbol{m}}(\boldsymbol{s})$, rather than its complex conjugate, is used for consistency with the nonconjugated coherent superposition in Eq. (10). The conjugate-symmetry relation in Eq. (18) shows that $\tilde{h}_{k,\boldsymbol{m}}$ is the expansion coefficient of $\bar{h}_k(\boldsymbol{s})$ with respect to the basis function $\Psi_{-\boldsymbol{m}}(\boldsymbol{s})$. Accordingly, Parseval's identity can be expressed as

$$\sum_{\boldsymbol{m}} \left| \tilde{h}_{k,\boldsymbol{m}} \right|^2 = \int_{S_R} \left| \bar{h}_k(\boldsymbol{s}) \right|^2 \mathrm{d}\boldsymbol{s}. \tag{23}$$

Substituting the WD expansions of the cascaded NF channel function and the reflection coefficient function into Eq. (10) yields the following expression for the effective channel gain of user k:

$$g_k = \sum_{\boldsymbol{m}} \tilde{h}_{k,\boldsymbol{m}} w_{\boldsymbol{m}}. \tag{24}$$

This representation converts the coherent superposition integral over the continuous aperture into a countably infinite sum in the WD. Further truncation is therefore required to obtain a finite-dimensional representation.

3.2. Low-Wavenumber Truncation and Energy Evaluation

Although the WD expansion contains infinitely many modes, retaining all of them is impractical for an XL-RIS. The controllable spatial degrees of freedom of the XL-RIS are limited by the number of reflecting elements, while the energy of the cascaded NF channel is typically concentrated within a bounded wavenumber region. Consequently, higher-order modes with low energy may contribute negligibly to the effective channel gain. On the XL-RIS aperture plane, the transverse wavenumber associated with the mode indexed by $\boldsymbol{m}$ can be expressed as

$$\boldsymbol{\kappa}_{\mathrm{t}}(\boldsymbol{m}) = \left[\frac{2\pi m_1}{L_y}, \frac{2\pi m_2}{L_z} \right]^{\mathrm{T}}, \tag{25}$$

where κ_y and κ_z denote the transverse wavenumber components along the y- and z-axes of the XL-RIS aperture, respectively. For propagating components in free space, the wavenumber component normal to the aperture must be real, which requires $\left\| \boldsymbol{\kappa}_{\mathrm{t}}(\boldsymbol{m}) \right\|_2 \le \kappa_0$. Accordingly, the normalized radial wavenumber is defined as

$$\rho(\boldsymbol{m}) = \frac{\left\| \boldsymbol{\kappa}_{\mathrm{t}}(\boldsymbol{m}) \right\|_2}{\kappa_0}, \tag{26}$$

where $\rho(\boldsymbol{m})$ denotes the magnitude of the two-dimensional transverse wavenumber vector divided by the free-space wavenumber. Modes satisfying $\rho(\boldsymbol{m}) \le 1$ lie within the propagating region, whereas those satisfying $\rho(\boldsymbol{m}) > 1$ correspond to evanescent components. For a given normalized truncation radius ρ_{c}, the finite set of retained wavenumber modes is defined as

$$\mathrm{M} = \left\{ \boldsymbol{m} = (m_1, m_2) \,|\, \rho(\boldsymbol{m}) \le \rho_{\mathrm{c}} \right\}, \tag{27}$$

where ρ_{c} denotes the normalized truncation radius. When $\rho_{\mathrm{c}}=1$, the retained wavenumber region coincides with the free-space propagating region. Smaller values retain only a subset of this region, whereas larger values extend the retained region beyond it.

The number of retained wavenumber modes is denoted by $N_{\mathrm{W}}=|\mathrm{M}|$. After the modes outside M are discarded, the effective channel gain for user k can be approximated as

$$\hat{g}_k=\sum_{\boldsymbol{m}\in\mathrm{M}}\tilde{h}_{k,\boldsymbol{m}}w_{\boldsymbol{m}}. \tag{28}$$

To quantify the channel energy retained after WD truncation, the WD energy spectrum averaged over all users is defined as

$$\bar{P}(\boldsymbol{m})=\frac{1}{K}\sum_{k=1}^{K}\left|\tilde{h}_{k,\boldsymbol{m}}\right|^2, \tag{29}$$

where $\bar{P}(\boldsymbol{m})$ denotes the channel energy averaged over all users for the wavenumber mode indexed by $\boldsymbol{m}$. The energy retention ratio for ρ_{c} is then defined as

$$\eta(\rho_{\mathrm{c}})=\frac{\sum_{\boldsymbol{m}\in\mathrm{M}}\bar{P}(\boldsymbol{m})}{\sum_{\boldsymbol{m}}\bar{P}(\boldsymbol{m})}, \tag{30}$$

where $\eta(\rho_{\mathrm{c}})$ denotes the fraction of the total WD channel energy retained within M. The normalized projection residual corresponding to the normalized truncation radius ρ_{c} can then be expressed as

$$e_{\mathrm{proj}}(\rho_{\mathrm{c}})=\sqrt{1-\eta(\rho_{\mathrm{c}})}. \tag{31}$$

To analyze the effect of truncation on each user, the energy retention ratio for user k is defined as

$$\eta_k(\rho_{\mathrm{c}})=\frac{\sum_{\boldsymbol{m}\in\mathrm{M}}\left|\tilde{h}_{k,\boldsymbol{m}}\right|^2}{\sum_{\boldsymbol{m}}\left|\tilde{h}_{k,\boldsymbol{m}}\right|^2}. \tag{32}$$

Based on this definition, the truncation-induced deviation in the effective channel gain admits the following upper bound.

Lemma 1: Let $E_k=\int_{\mathrm{S_R}}\left|\bar{\boldsymbol{h}}_k(\boldsymbol{s})\right|^2\mathrm{d}\boldsymbol{s}$ denote the channel energy of user k. Under the constant-modulus constraint, the resulting truncation error in the effective channel gain satisfies $\left|g_k-\hat{g}_k\right|\le\sqrt{(1-\eta_k)E_kA_{\mathrm{R}}}$.

Proof: See Appendix A.

Fig. 1 illustrates the WD energy distribution and the corresponding energy retention characteristics of the cascaded NF channel. Fig. 1(a) shows that most of the channel energy is concentrated near the origin in the normalized WD, indicating the dominance of low-wavenumber modes. The black dashed circle marks the truncation boundary corresponding to $\rho_{\mathrm{c}}=1$. Fig. 1(b) shows the energy retention ratio as a function of the normalized truncation radius. The ratio increases rapidly with the radius and gradually levels off beyond $\rho_{\mathrm{c}}=1$. Specifically, it reaches 90% and 95% at $\rho_{\mathrm{c}}=0.26$ and $\rho_{\mathrm{c}}=0.54$, respectively, and approximately 97.4% at $\rho_{\mathrm{c}}=1$. These results demonstrate that a finite set of low-wavenumber modes captures most of the WD channel energy, supporting the use of low-wavenumber truncation for subsequent low-complexity multi-beam design.

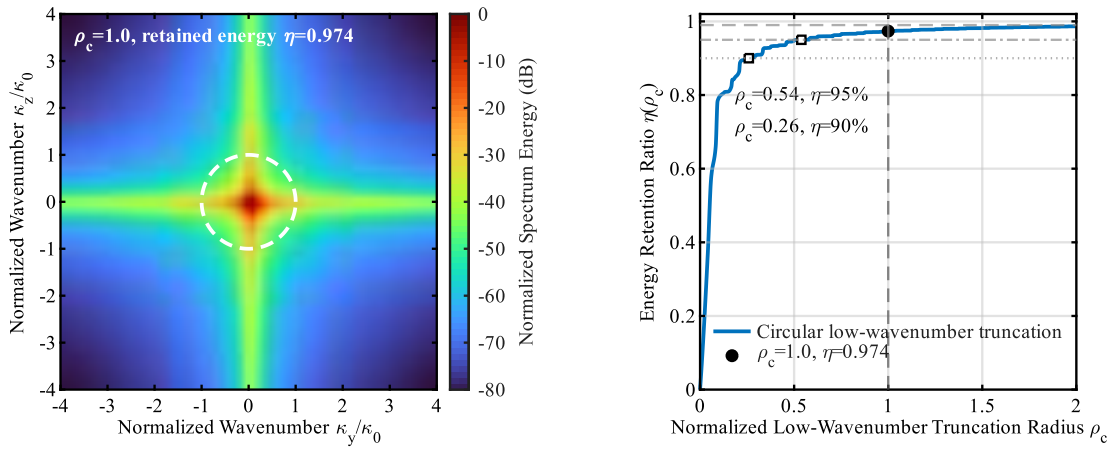


Fig. 1 Low-Wavenumber Truncation Characteristics

These results demonstrate that the energy of the cascaded NF channel is concentrated in a limited region of the WD, supporting the use of low-wavenumber truncation. Restricting the mode set to M enables the subsequent multi-beam optimization to be formulated using a finite-dimensional equivalent design matrix, reducing the representation dimension and computational complexity while retaining most of the channel energy.

3.3. Finite-Dimensional Wavenumber-Domain Representation

Once M and N_{W} are determined, the cascaded NF channel can be approximated using a finite set of WD projection coefficients. To facilitate matrix representation, the two-dimensional mode indices in M are arranged in a fixed order as $\boldsymbol{m}^{(1)},\ldots,\boldsymbol{m}^{(N_{\mathrm{W}})}$, establishing a one-to-one correspondence between each two-dimensional mode index and its scalar index. For user k, the channel projection coefficients corresponding to these ordered modes are collected into the vector $\tilde{\boldsymbol{h}}_{k,\boldsymbol{m}}$. The vectors for all K users are then stacked row-wise to form the following matrix:

$$\tilde{\boldsymbol{H}}=\left[\tilde{\boldsymbol{h}}_1,\ldots,\tilde{\boldsymbol{h}}_K\right]^{\mathrm{T}}\in\mathbb{C}^{K\times N_{\mathrm{W}}}, \tag{33}$$

where $\tilde{\boldsymbol{H}}$ denotes the multiuser WD channel projection matrix. For a discrete XL-RIS comprising N reflecting elements, the Fourier basis functions defined in Eq. (18) are sampled at the element centers to construct the weighted discrete Fourier basis matrix $\boldsymbol{\Psi}\in\mathbb{C}^{N\times N_{\mathrm{W}}}$, whose (n,j)-th entry is $\left[\boldsymbol{\Psi}\right]_{n,j}=A_{\mathrm{e}}\Psi_{\boldsymbol{m}^{(j)}}\left(\boldsymbol{s}_n\right)$. The WD reflection coefficient vector can then be expressed as

$$\boldsymbol{w}=\boldsymbol{\Psi}^{\mathrm{H}}\boldsymbol{q}. \tag{34}$$

Let $\bar{\boldsymbol{H}}=\left[\bar{\boldsymbol{h}}_1,\cdots,\bar{\boldsymbol{h}}_K\right]\in\mathbb{C}^{N\times K}$ denote the sampled cascaded channel matrix in the spatial domain, where $\bar{\boldsymbol{h}}_k$ collects the channel samples for user k across the XL-RIS elements. Similarly, the multiuser WD channel projection matrix can be expressed as

$$\tilde{\boldsymbol{H}}=\bar{\boldsymbol{H}}^{\mathrm{T}}\boldsymbol{\Psi}. \tag{35}$$

3.4. Wavenumber-Domain Equivalent Design Matrix

According to Eq. (28), the truncated effective channel gain for each user is expressed as a sum over all retained

modes. Each term is the product of the corresponding WD projection coefficient of the cascaded NF channel function and the expansion coefficient of the reflection coefficient function. Stacking the truncated effective channel gains for all users yields the following WD representation:

$$\hat{\boldsymbol{g}} = \tilde{\boldsymbol{H}}\boldsymbol{w}, \tag{36}$$

where $\hat{\boldsymbol{g}} = \left[\hat{g}_1, \ldots, \hat{g}_K\right]^{\mathrm{T}}$ denotes the vector of truncated effective channel gains for all users. Substituting Eq. (34) into Eq. (36) yields the following expression for this vector:

$$\hat{\boldsymbol{g}} = \tilde{\boldsymbol{H}}\boldsymbol{\Psi}^{\mathrm{H}}\boldsymbol{q}, \tag{37}$$

Under the passive lossless reflection model, the reflection coefficient of each XL-RIS element must satisfy $\left|q_n\right| = 1$. The WD coefficient vector $\boldsymbol{w}$ is obtained by projecting the spatial-domain reflection coefficient vector $\boldsymbol{q}$ onto the WD basis. The WD coefficients are therefore subject to the constraints induced by the spatial-domain constant-modulus condition. Accordingly, the spatial-domain reflection coefficient vector is retained as the optimization variable. To incorporate the spherical-wave characteristics of NF propagation into this formulation, the WD equivalent design matrix is defined as

$$\boldsymbol{C} = \boldsymbol{\Psi}\tilde{\boldsymbol{H}}^{\mathrm{H}}, \tag{38}$$

Where $\boldsymbol{C} \in \mathbb{C}^{N \times K}$. Accordingly, the effective reflection gain vector of the K users can be rewritten as

$$\hat{\boldsymbol{g}} = \boldsymbol{C}^{H}\boldsymbol{q}, \tag{39}$$

where $\boldsymbol{C}$ denotes the WD equivalent design matrix, which linearly maps the spatial-domain XL-RIS reflection coefficient vector $\boldsymbol{q}$ to the vector of truncated effective channel gains for all users. Equation (39) provides a finite-dimensional matrix approximation of the continuous-aperture NF integral formulation. In this representation, the truncated effective channel gain for user k is obtained by coherently combining the contributions from all XL-RIS elements. Constructed through WD projection, $\boldsymbol{C}$ captures the NF propagation characteristics and enables multi-beam optimization of the XL-RIS phase shifts under the constant-modulus constraint.

4. Multi-user Multi-beam Design

The multi-beam optimization problem is solved using the BCD-MM framework adopted in [9]. The proposed method differs from that in [9] primarily in the construction of the design matrix. In [9], this matrix is constructed by arranging NF codewords defined on a discrete spatial grid as columns, which may introduce codebook quantization errors. In contrast, the proposed method uses the WD equivalent design matrix $\boldsymbol{C}$. The resulting truncation-induced error in the effective channel gain is bounded in terms of the energy retention ratio.

4.1. Multi-Beam Optimization Model

Using the truncated WD representation of the effective channel gain vector for all users, the fairness-oriented target-gain matching surrogate problem is approximated by the following finite-dimensional problem:

$$\begin{aligned} \mathrm{P}_2 : &\min_{\boldsymbol{q},\boldsymbol{\zeta}} \left\| \bar{\boldsymbol{g}} - \boldsymbol{C}^{\mathrm{H}}\boldsymbol{q} \right\|_2^2, \\ \text{s.t.} &\left|q_n\right| = 1, \forall n, \left|\zeta_k\right| = 1, \forall k \end{aligned} \tag{40}$$

The resulting problem is a nonconvex quadratic program because of the constant-modulus constraints. Let $L = \left\| \bar{\boldsymbol{g}} - \boldsymbol{C}^{\mathrm{H}}\boldsymbol{q} \right\|_2^2$ denote the squared Euclidean norm of the gain-matching error vector. Expanding L yields

$$L=\bar{\boldsymbol{g}}^{\mathrm{H}}\bar{\boldsymbol{g}}+\boldsymbol{q}^{\mathrm{H}}\boldsymbol{C}\boldsymbol{C}^{\mathrm{H}}\boldsymbol{q}-2\mathrm{Re}\left\{\bar{\boldsymbol{g}}^{\mathrm{H}}\boldsymbol{C}^{\mathrm{H}}\boldsymbol{q}\right\}, \tag{41}$$

where the first term is independent of the optimization variable $\boldsymbol{q}$ and can therefore be omitted without affecting the optimal solution. Accordingly, the optimization problem can be equivalently expressed as

$$\begin{aligned}\mathrm{P}_q:\min_{\boldsymbol{q}} L&=\boldsymbol{q}^{\mathrm{H}}\boldsymbol{C}\boldsymbol{C}^{\mathrm{H}}\boldsymbol{q}-2\mathrm{Re}\left\{\bar{\boldsymbol{g}}^{\mathrm{H}}\boldsymbol{C}^{\mathrm{H}}\boldsymbol{q}\right\}\\ \text{s.t.}&\left|q_n\right|=1\end{aligned} \tag{42}$$

Since $\boldsymbol{C}\in\mathbb{C}^{N\times K}$, the quadratic coefficient matrix $\boldsymbol{C}\boldsymbol{C}^{\mathrm{H}}$ has rank at most K. For the considered XL-RIS system with $K\ll N$, this low-rank structure can be exploited to compute the largest eigenvalue required for the subsequent MM update.

For notational simplicity, define $\boldsymbol{F}=\boldsymbol{C}\boldsymbol{C}^{\mathrm{H}}$ and $\boldsymbol{b}=\boldsymbol{C}\bar{\boldsymbol{g}}$. These quantities denote the Hermitian positive semidefinite quadratic coefficient matrix and the target-dependent linear coefficient vector in the objective function, respectively. The objective function of P_q can then be rewritten as

$$\begin{aligned}\mathrm{P}_q:\min_{\boldsymbol{q}} L&=\boldsymbol{q}^{\mathrm{H}}\boldsymbol{F}\boldsymbol{q}-2\mathrm{Re}\left\{\boldsymbol{b}^{\mathrm{H}}\boldsymbol{q}\right\}.\\ \text{s.t.}&\left|q_n\right|=1\end{aligned} \tag{43}$$

4.2. MM Update of the XL-RIS Reflection Coefficient Vector

Following the BCD framework, the XL-RIS reflection coefficient vector $\boldsymbol{q}$ and the auxiliary phase-factor vector $\boldsymbol{\zeta}$ are updated alternately. With $\boldsymbol{\zeta}$ fixed, the subproblem with respect to $\boldsymbol{q}$ remains nonconvex because of the constant-modulus constraint. To obtain a tractable update, the MM method is used to construct an upper bound on the quadratic objective at the current iterate $\boldsymbol{q}^t$. Specifically, the majorization matrix is chosen as $\boldsymbol{U}=\lambda_{\max}\boldsymbol{I}_N$, where $\lambda_{\max}$ denotes the largest eigenvalue of $\boldsymbol{F}$ and $\boldsymbol{I}_N$ denotes the $N\times N$ identity matrix. Since $\boldsymbol{U}-\boldsymbol{F}\succeq\boldsymbol{0}$, the quadratic term $\boldsymbol{q}^{\mathrm{H}}\boldsymbol{F}\boldsymbol{q}$ can be majorized at $\boldsymbol{q}^t$ using $\boldsymbol{U}$, yielding the following surrogate function:

$$\mu\left(\boldsymbol{q}\,|\,\boldsymbol{q}^t\right)=\boldsymbol{q}^{\mathrm{H}}\boldsymbol{U}\boldsymbol{q}+2\mathrm{Re}\left\{\boldsymbol{q}^{\mathrm{H}}\left(\boldsymbol{F}-\boldsymbol{U}\right)\boldsymbol{q}^t\right\}+\left(\boldsymbol{q}^t\right)^{\mathrm{H}}\left(\boldsymbol{U}-\boldsymbol{F}\right)\boldsymbol{q}^t-2\mathrm{Re}\left\{\boldsymbol{b}^{\mathrm{H}}\boldsymbol{q}\right\}, \tag{44}$$

where $\mu\left(\boldsymbol{q}\,|\,\boldsymbol{q}^t\right)$ denotes the surrogate function constructed at the current iterate $\boldsymbol{q}^t$. The surrogate function in Eq. (44) satisfies the standard MM conditions: the upper-bound condition $L\left(\boldsymbol{q}\right)\le\mu\left(\boldsymbol{q}\,|\,\boldsymbol{q}^t\right)$, the tangency condition $L\left(\boldsymbol{q}^t\right)=\mu\left(\boldsymbol{q}^t\,|\,\boldsymbol{q}^t\right)$, and the first-order consistency condition $\nabla L\left(\boldsymbol{q}^t\right)=\nabla\mu\left(\boldsymbol{q}\,|\,\boldsymbol{q}^t\right)\big|_{\boldsymbol{q}=\boldsymbol{q}^t}$. Under the constant-modulus constraint, $\boldsymbol{q}^{\mathrm{H}}\boldsymbol{q}=N$ holds. Consequently, the quadratic term involving $\boldsymbol{U}$ simplifies to

$$\boldsymbol{q}^{\mathrm{H}}\boldsymbol{U}\boldsymbol{q}=\lambda_{\max}N. \tag{45}$$

Similarly, $\left(\boldsymbol{q}^t\right)^{\mathrm{H}}\left(\boldsymbol{U}-\boldsymbol{F}\right)\boldsymbol{q}^t$ is independent of $\boldsymbol{q}$ during iteration $\left(t+1\right)$. After omitting all terms independent of $\boldsymbol{q}$, the surrogate function simplifies to

$$\mu\left(\boldsymbol{q}\,|\,\boldsymbol{q}^t\right)\propto-2\mathrm{Re}\left\{\boldsymbol{q}^{\mathrm{H}}\left(\boldsymbol{b}-\boldsymbol{F}\boldsymbol{q}^t+\lambda_{\max}\boldsymbol{q}^t\right)\right\}. \tag{46}$$

Define $\boldsymbol{v}^t=\boldsymbol{b}-\boldsymbol{F}\boldsymbol{q}^t+\lambda_{\max}\boldsymbol{q}^t$, $\boldsymbol{v}^t\in\mathbb{C}^{N\times1}$. Accordingly, the MM subproblem at iteration $\left(t+1\right)$ can be written as

$$\boldsymbol{q}^{t+1}=\arg\min_{\left|q_n\right|=1}-2\mathrm{Re}\left\{\boldsymbol{q}^{\mathrm{H}}\boldsymbol{v}^t\right\}. \tag{47}$$

Under the constant-modulus constraint, the objective function in Eq. (47) is minimized by aligning the phase

of each reflection coefficient q_n with that of the corresponding auxiliary vector entry v_n^t. This yields the following closed-form update for the XL-RIS reflection coefficient vector:

$$\boldsymbol{q}^{t+1} = \exp\left(\mathrm{j}\angle\left(\boldsymbol{C}\bar{\boldsymbol{g}} - \boldsymbol{C}\boldsymbol{C}^{\mathrm{H}}\boldsymbol{q}^t + \lambda_{\max}\boldsymbol{q}^t\right)\right), \tag{48}$$

where $\exp\left(\mathrm{j}\angle[\cdot]\right)$ denotes the element-wise projection onto the unit circle, which preserves the phase of each nonzero vector entry.

4.3. Closed-Form Update of the Target Phase Factors

With the XL-RIS reflection coefficient vector fixed, the auxiliary phase-factor vector is updated by solving a separate subproblem. Since the prescribed targets specify only the effective channel gain magnitudes, the target phases can be treated as auxiliary degrees of freedom. Accordingly, the subproblem for the auxiliary phase-factor vector can be expressed as

$$\begin{aligned} &\mathrm{P}_{\boldsymbol{\zeta}}: \min_{\boldsymbol{\zeta}} \left\| \boldsymbol{g}_0 \odot \boldsymbol{\zeta} - \boldsymbol{C}^{\mathrm{H}}\boldsymbol{q} \right\|_2^2. \\ &\text{s.t.} \left|\zeta_k\right| = 1, k \in \{1, \cdots, K\} \end{aligned} \tag{49}$$

Since the objective function in Eq. (49) is separable across the entries of the auxiliary phase-factor vector $\boldsymbol{\zeta}$, the problem can be decomposed into K independent scalar subproblems, one for each user, as follows:

$$\min_{|\zeta_k|=1} \left\| g_{0,k}\zeta_k - g_k \right\|_2^2 = g_{0,k}^2 + \left|g_k\right|^2 - 2g_{0,k}\mathrm{Re}\left\{\zeta_k^* g_k\right\}. \tag{50}$$

Under $\left|\zeta_k\right| = 1$ and $g_{0,k} > 0$, the minimum is attained when the phase of ζ_k is aligned with that of $\hat{g}_k$. Collecting the resulting phase factors into a vector yields the following closed-form update:

$$\boldsymbol{\zeta}^{t+1} = \exp\left(\mathrm{j}\angle\left(\boldsymbol{C}^{\mathrm{H}}\boldsymbol{q}\right)\right). \tag{51}$$

Accordingly, the target effective-gain vector is updated as $\bar{\boldsymbol{g}}^{t+1} = \boldsymbol{g}_0 \odot \boldsymbol{\zeta}^{t+1}$.

4.4. Complexity Analysis

The MM update requires the largest eigenvalue $\lambda_{\max} = \lambda_{\max}\left(\boldsymbol{C}\boldsymbol{C}^{\mathrm{H}}\right)$. Without exploiting the low-rank structure of the $N \times N$ quadratic coefficient matrix $\boldsymbol{C}\boldsymbol{C}^{\mathrm{H}}$, computing this eigenvalue via a full eigenvalue decomposition (EVD) incurs a computational complexity of $\mathrm{O}\left(N^3\right)$. In typical multiuser XL-RIS scenarios, $K \ll N$ holds, making $\boldsymbol{C}$ a tall matrix. Consequently, $\mathrm{rank}\left(\boldsymbol{C}\boldsymbol{C}^{\mathrm{H}}\right) \le K$, implying that $\boldsymbol{C}\boldsymbol{C}^{\mathrm{H}}$ has at most K nonzero eigenvalues. Since $\boldsymbol{C}\boldsymbol{C}^{\mathrm{H}}$ and $\boldsymbol{C}^{\mathrm{H}}\boldsymbol{C}$ are both Hermitian positive semidefinite and share the same nonzero eigenvalues, their largest eigenvalues satisfy

$$\lambda_{\max}\left(\boldsymbol{C}\boldsymbol{C}^{\mathrm{H}}\right) = \lambda_{\max}\left(\boldsymbol{T}\right), \tag{52}$$

where $\boldsymbol{T} = \boldsymbol{C}^{\mathrm{H}}\boldsymbol{C}$, $\boldsymbol{T} \in \mathbb{C}^{K \times K}$ denotes the Gram matrix of the equivalent design matrix. Since $\boldsymbol{C}\boldsymbol{C}^{\mathrm{H}}$ and $\boldsymbol{C}^{\mathrm{H}}\boldsymbol{C}$ share the same nonzero eigenvalues, computing the largest eigenvalue via a full EVD of the smaller Gram matrix reduces the EVD complexity from $\mathrm{O}\left(N^3\right)$ to $\mathrm{O}\left(K^3\right)$. Forming $\boldsymbol{T}$ requires $\mathrm{O}\left(NK^2\right)$ operations. For a given channel realization, $\boldsymbol{C}$ remains fixed, so its largest eigenvalue needs to be computed only once before the BCD-MM iterations begin. Moreover, the dominant matrix–vector product $\boldsymbol{C}\boldsymbol{C}^{\mathrm{H}}\boldsymbol{q}^t$ in Eq. (52) can be evaluated as $\boldsymbol{C}\left(\boldsymbol{C}^{\mathrm{H}}\boldsymbol{q}^t\right)$ with a computational complexity of $\mathrm{O}\left(NK\right)$, avoiding the explicit construction of $\boldsymbol{C}\boldsymbol{C}^{\mathrm{H}}$. Thus, the dominant

computational complexity of each BCD-MM iteration is $\mathrm{O}\left(NK\right)$. The overall computational complexity, including the construction of the WD equivalent design matrix $\boldsymbol{C}$, the formation of the Gram matrix $\boldsymbol{T}$, the computation of the largest eigenvalue, and all BCD-MM iterations, can be expressed as

$$\mathrm{O}_{\text{total}} = \mathrm{O}\left(KNN_{\mathrm{W}}\right) + \mathrm{O}\left(NK^2\right) + \mathrm{O}\left(K^3\right) + \mathrm{O}\left(I_{\mathrm{BCD}}NK\right) \tag{53}$$

where I_{BCD} denotes the number of BCD-MM iterations. For XL-RIS elements arranged on a uniform rectangular grid, the WD projection can be efficiently implemented using a two-dimensional fast Fourier transform (FFT). Moreover, low-wavenumber truncation reduces the number of retained modes N_{W}. Lemma 1 provides an upper bound on the resulting truncation error. This error can be controlled by adjusting ρ_{c}.

5. Simulation Results and Discussion

This section evaluates the statistical worst-user performance, reliability, and convergence behavior of the proposed design and examines the effects of key system and WD parameters.

5.1. Statistical and Convergence Performance Metrics

Since the user locations and the corresponding cascaded channels vary across independent Monte Carlo realizations, the resulting minimum user spectral efficiency (SE), $R_{\min}$, is a random variable. Its statistical distribution is therefore characterized using the empirical cumulative distribution function (CDF), which can be expressed as

$$\hat{F}_{R_{\min}}\left(z\right) = \frac{1}{N_{\mathrm{MC}}}\sum_{\ell=1}^{N_{\mathrm{MC}}} 1\left\{R_{\min}^{\ell} \le \xi\right\}, \tag{54}$$

where N_{MC} denotes the total number of independent Monte Carlo realizations, ℓ denotes the realization index, $R_{\min}^{\ell}$ denotes the minimum user SE in the corresponding realization, ξ denotes a generic SE level, and $1\{\cdot\}$ denotes the indicator function. To further characterize the lower-tail performance of $R_{\min}$, the ε-outage minimum user SE is defined as

$$R_{\min}^{\varepsilon} = \inf\left\{\xi : \hat{F}_{R_{\min}}\left(\xi\right) \ge \varepsilon\right\}, \tag{55}$$

where $\varepsilon \in \left(0,1\right)$ denotes the prescribed outage probability and $\inf\{\cdot\}$ denotes the infimum. Within the outage-rate framework for quasi-static random channels, an outage probability of 10% is selected to characterize lower-tail performance. The corresponding 10%-outage minimum user SE is exceeded in approximately 90% of the channel realizations. With 600 independent Monte Carlo realizations, approximately 60 samples contribute to the evaluation of the lower 10% tail. To quantify the probability of meeting a prescribed minimum user SE requirement, the empirical satisfaction probability is defined as

$$\hat{P}_{\mathrm{sat}}\left(R_{\mathrm{th}}\right) = \frac{1}{N_{\mathrm{MC}}}\sum_{\ell=1}^{N_{\mathrm{MC}}} 1\left\{R_{\min}^{\ell} \ge R_{\mathrm{th}}\right\}, \tag{56}$$

where R_{th} denotes the prescribed minimum user SE threshold. Since $R_{\min}^{\ell}$ denotes the minimum SE across all users in realization ℓ-th, the condition $R_{\min}^{\ell} \ge R_{\mathrm{th}}$ indicates that all users meet the prescribed requirement. To characterize the convergence behavior of the proposed BCD-MM algorithm, the mean normalized matching error is defined as

$$\bar{J}_{\mathrm{norm}}^{t}=\frac{1}{N_{\mathrm{MC}}}\sum_{\ell=1}^{N_{\mathrm{MC}}}\frac{J_{\ell}^{t}}{J_{\ell}^{0}}, \tag{57}$$

where J_{ℓ}^{t} denotes the value of the gain-matching objective at iteration t in Monte Carlo realization ℓ-th, and J_{ℓ}^{0} denotes its initial value in the same realization. The mean normalized matching error is obtained by dividing the objective value by its initial value in each realization and then averaging over all realizations. A smaller value indicates a smaller gain-matching error relative to the initial mismatch.

Together, the empirical CDF, ε-outage minimum user SE, and empirical satisfaction probability characterize worst-user performance and reliability across channel realizations. The mean normalized matching error tracks the convergence behavior of the BCD-MM algorithm.

5.2. Simulation Setup and Performance Evaluation

To evaluate the effectiveness of the proposed method, four benchmark schemes are considered. The NF codebook-based BCD-MM benchmark [9] constructs the design matrix from NF codewords and solves the multi-beam design problem under the constant-modulus constraint of the passive XL-RIS. This benchmark differs from the proposed method primarily in the channel representation. The NF single-beam design based on [3] uses angle–distance NF codewords to focus a beam on each user individually. The FF single-beam design [3] uses angular-domain DFT codewords constructed under the plane-wave assumption. The random-phase benchmark assigns random phase shifts to the XL-RIS elements. The main simulation parameters are summarized in Table 2.

Table 2. Simulation Parameters for the Near-Field Scenario

Parameter	Value
Carrier frequency	$f=7GHz$
Wavelength	$\lambda=0.0429m$
Number of XL-RIS elements (horizontal/vertical)	$N_1=64, N_2=8$
XL-RIS width	$L_y=1.371\mathrm{m}$
XL-RIS height	$L_z=0.171\mathrm{m}$
XL-RIS center position	$(0,0,0)$
BS and user distribution region	$R_x=[120\lambda,420\lambda]$
BS and user distribution region	$R_y=[-120\lambda,120\lambda]$
BS and user distribution region	$R_z=[-40\lambda,40\lambda]$
User-to-XL-RIS distance	$r\in[5.14,18.80]\mathrm{m}$
Rayleigh distance	$R_{\mathrm{Ray}}=89.14\mathrm{m}$
Number of retained wavenumber modes	$N_{\mathrm{W}}=383$
Maximum BCD–MM iterations	200
Stopping threshold	10^{-4}
Default wavenumber truncation radius	1.00

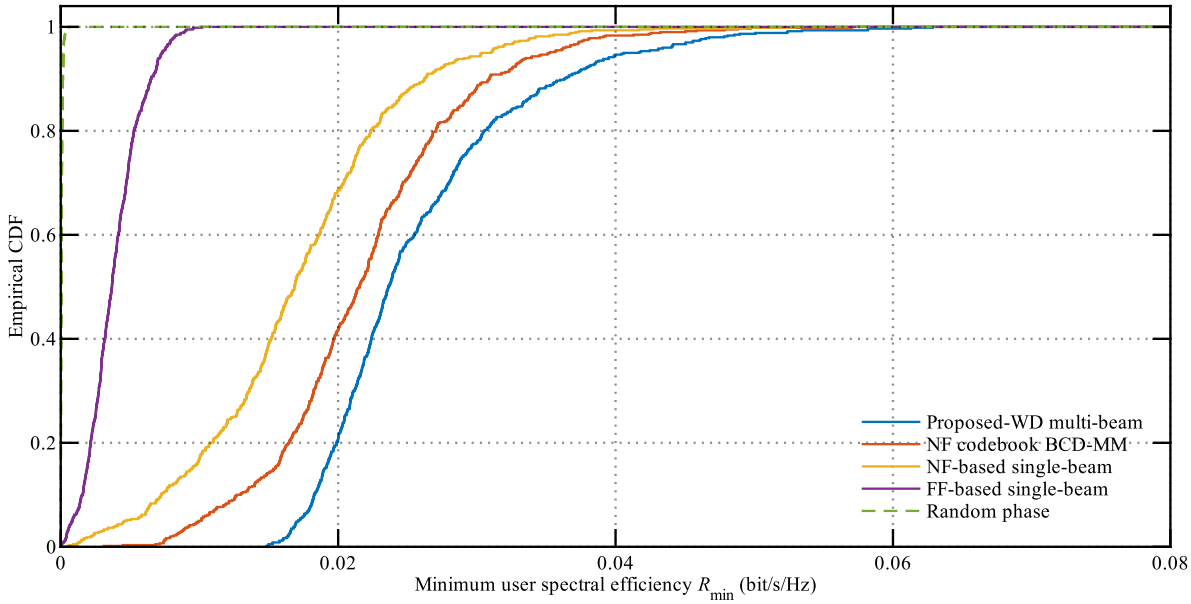


Fig. 2 Statistical Distribution of the Minimum User Spectral Efficiency.

Fig. 2 shows the empirical CDF of the minimum user SE at an SNR of 0dB. A rightward shift of the CDF indicates improved worst-user performance. The proposed WD multi-beam scheme exhibits the most favorable distribution among the considered schemes. At $R_{\min} = 0.02$ bit/s/Hz, its empirical CDF is approximately 0.2083, compared with 0.4200 and 0.6850 for the NF codebook-based BCD-MM and NF single-beam schemes, respectively. Equivalently, approximately 79.17% of the realizations under the proposed scheme achieve a minimum user SE above 0.020 bit/s/Hz, indicating a higher probability of exceeding this threshold than under either benchmark. Moreover, the proposed scheme achieves a mean minimum user SE of 0.0258 bit/s/Hz, approximately 17.7% higher than the 0.0219 bit/s/Hz achieved by the NF codebook-based BCD-MM scheme, the best-performing benchmark in terms of this metric. This performance gain may be attributed to the WD representation, which captures the distance-dependent structure of the NF channels and facilitates multiuser beam focusing under the constant-modulus constraint.

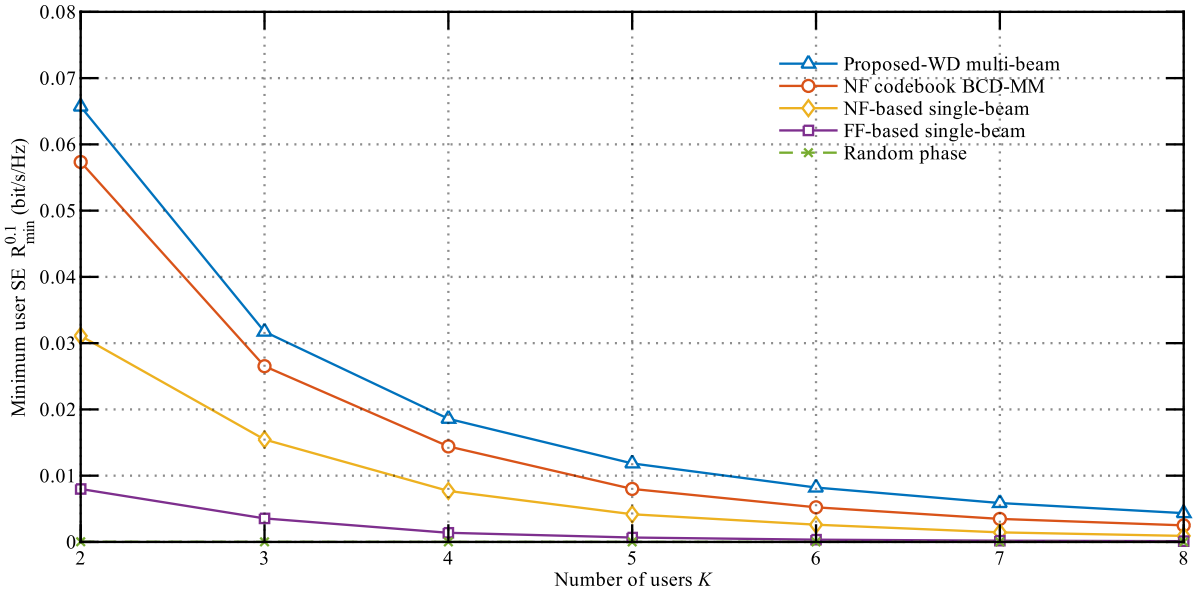
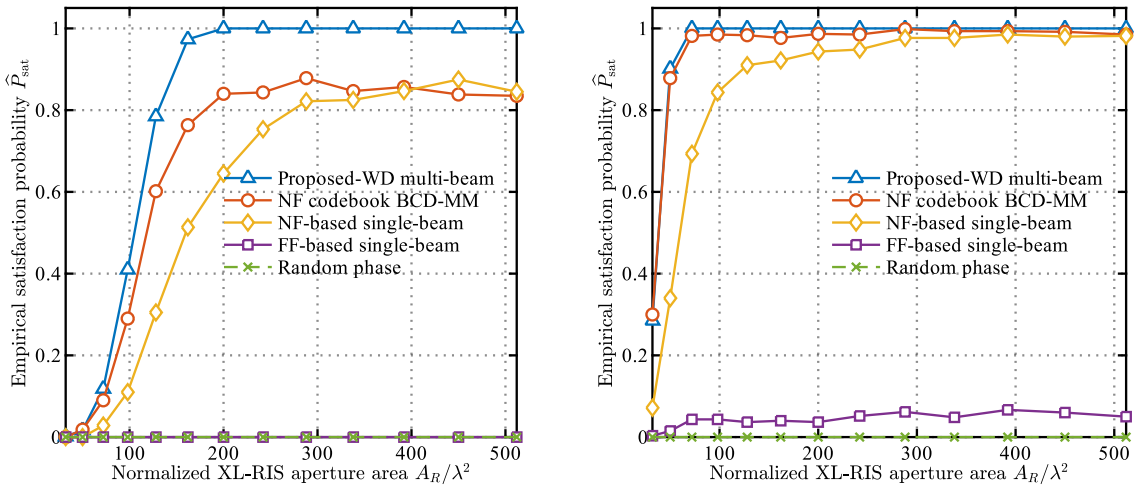


Fig. 3. Minimum User SE Versus Number of Users.

Fig. 3 shows the 10%-outage minimum user SE as a function of the number of users K. The proposed WD multi-beam scheme consistently achieves the highest values of this metric among all considered schemes. For

example, at $K=4$, the proposed scheme achieves $R_{\min}^{0.1} \approx 0.0186$ bit/s/Hz, approximately 29.2% higher than that achieved by the NF codebook-based BCD-MM benchmark. The NF single-beam, FF single-beam, and random-phase schemes achieve successively lower values. As K increases, the 10%-outage minimum user SE decreases because each user is allocated a smaller fraction $1/K$ of the available transmission time and the shared XL-RIS reflection profile must accommodate the beam-focusing requirements of more users. The performance advantage of the proposed scheme across the considered user counts suggests that the WD representation enables the multi-beam design to exploit the NF channel structure more effectively, thereby improving worst-user performance at the prescribed outage probability.



(a) $R_{\text{th}} = 0.0200$ bit/s/Hz (b) $R_{\text{th}} = 0.0075$ bit/s/Hz

Fig. 4. Satisfaction Probability Versus Normalized XL-RIS Aperture Area.

Fig. 4 shows the empirical satisfaction probability as a function of the normalized XL-RIS aperture area for two minimum user SE thresholds. In Fig. 4(a), the stricter threshold of $R_{\text{th}} = 0.0200$ bit/s/Hz is used to highlight reliability differences among the schemes. This subfigure evaluates the ability of each design to meet a relatively demanding worst-user SE requirement as the aperture area increases. The satisfaction probability of the proposed WD scheme increases rapidly with the aperture area, as a larger aperture enhances coherent reflection and facilitates more effective NF beam focusing. At $A_{\text{R}}/\lambda = 200$, the empirical satisfaction probability of the proposed scheme reaches 1, compared with approximately 0.840 and 0.645 for the NF codebook-based BCD-MM and NF single-beam schemes, respectively, corresponding to absolute improvements of 16.0 and 35.5 percentage points. The corresponding probabilities for the FF single-beam and random-phase schemes remain zero. Fig. 4(b) uses a lower threshold of $R_{\text{th}} = 0.0075$ bit/s/Hz to further examine these two schemes. This relaxed threshold helps distinguish failure to meet the stricter SE requirement from an inability to achieve positive SE. At the same aperture area, the proposed scheme again achieves an empirical satisfaction probability of 1, whereas that of the FF single-beam scheme is approximately 0.037. This nonzero probability confirms that the FF scheme can achieve positive SE, although none of the evaluated realizations meets the stricter requirement in Fig. 4(a). Overall, these results suggest that the proposed WD design effectively exploits the distance-dependent NF channel structure and the enlarged aperture to improve the reliability of meeting the prescribed minimum user SE requirements.

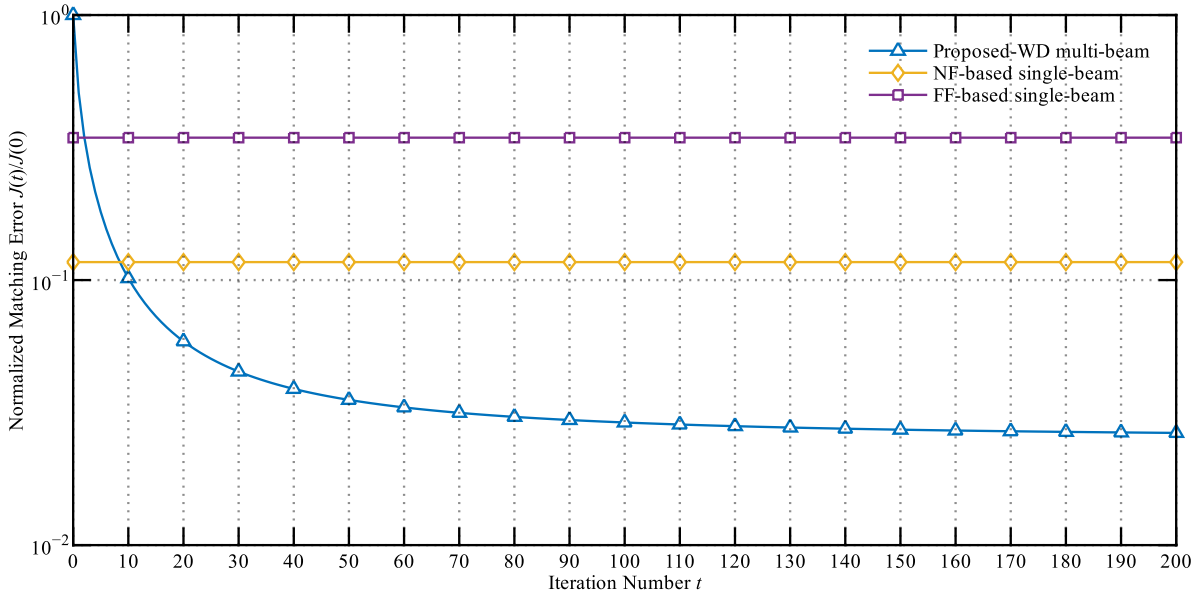


Fig. 5. Statistical Convergence Performance Versus BCD-MM Iteration.

Fig. 5 shows the mean normalized matching error as a function of the BCD-MM iteration index. A lower value indicates a smaller gain-matching error relative to the initial mismatch. For the proposed WD multi-beam scheme, this metric decreases rapidly during the early iterations and then gradually approaches a stable value. For example, at $t = 20$, it is approximately 0.0587, which is approximately 49.8% and 83.0% lower than the corresponding values for the NF single-beam and FF single-beam schemes, respectively. In contrast, the curves for these two single-beam schemes remain constant because their reflection coefficients are not updated during the iterations. These curves therefore serve as fixed reference levels. The NF single-beam scheme achieves a lower mean normalized matching error than the FF single-beam scheme because spherical-wave focusing better captures the distance-dependent phase characteristics of NF channels. Overall, these results illustrate that the mean normalized matching error of the proposed WD multi-beam scheme stabilizes during the BCD-MM iterations and remains lower than those of the two single-beam benchmarks.

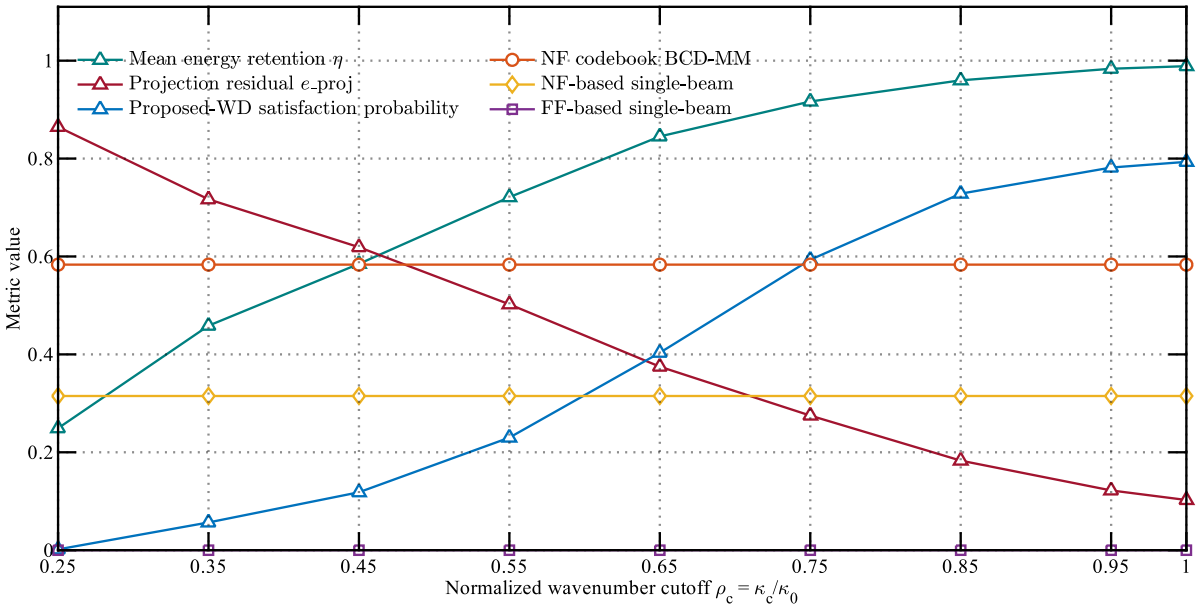


Fig. 6. Impact of the normalized wavenumber cutoff on representation accuracy and reliability.

Fig. 6 shows the effects of the normalized wavenumber cutoff on WD representation accuracy and communication reliability. The triangular markers indicate the mean energy retention ratio, mean normalized

projection residual, and empirical satisfaction probability of the proposed WD scheme. The circular, diamond, and square markers indicate the empirical satisfaction probabilities of the three benchmark schemes. As ρ_c increases, more wavenumber modes are retained, resulting in a higher mean energy retention ratio and a lower mean normalized projection residual. These changes improve the accuracy of the truncated WD representation. For example, at $\rho_c = 0.75$, the proposed WD scheme achieves an empirical satisfaction probability of 59.3%, corresponding to relative improvements of approximately 1.7% and 88.3% over the NF codebook-based BCD-MM and NF single-beam schemes, respectively. Compared with the FF single-beam scheme, whose empirical satisfaction probability is zero, the proposed scheme achieves an absolute increase of 59.3 percentage points. At the same cutoff, the mean energy retention ratio reaches approximately 91.7%, while the mean normalized projection residual decreases to approximately 27.5%. These results suggest that retaining sufficient dominant WD modes supports accurate channel representation and effective multiuser beam focusing, thereby increasing the probability of meeting the prescribed minimum user SE requirement.

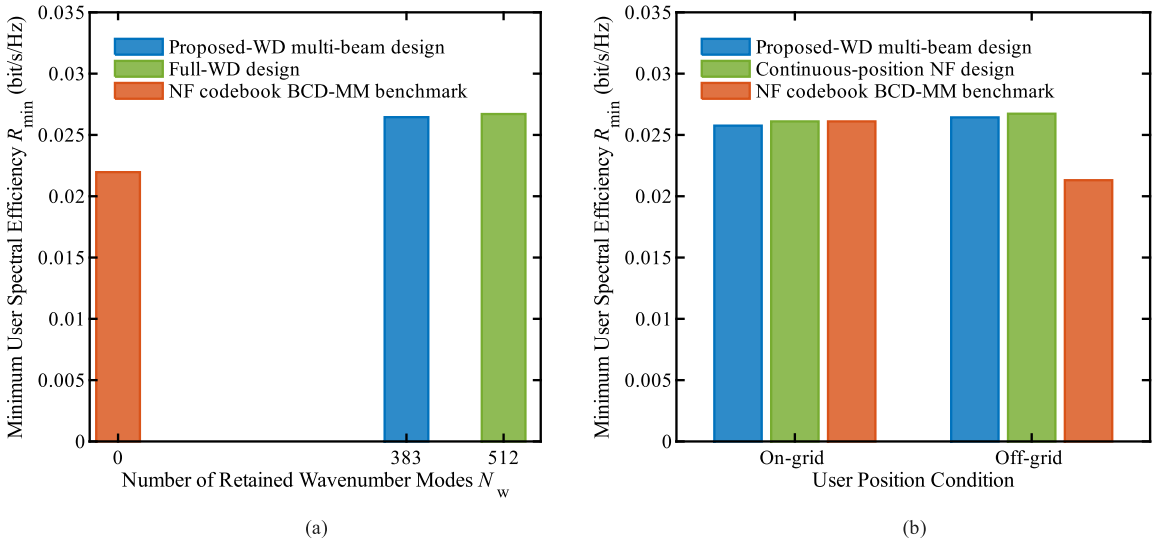


Fig. 7. Ablation comparison of different near-field multi-beam design schemes.

Fig. 7 presents an ablation study of different NF multi-beam designs to examine the source of the performance gain achieved by the proposed method. In Fig. 7(a), the full WD design, the proposed truncated WD design, and the NF codebook-based BCD-MM scheme achieve minimum user SEs of 0.02671, 0.02645, and 0.02196 bit/s/Hz, respectively. The full and truncated WD designs retain 512 and 383 wavenumber modes, respectively. The codebook-based scheme does not involve WD truncation and is plotted at $N_W = 0$ solely for comparison. The proposed truncated WD design incurs a performance loss of approximately 0.97% relative to the full WD design while achieving a gain of approximately 20.45% over the NF codebook-based BCD-MM scheme. These results indicate that truncation preserves most of the performance advantage offered by the WD representation. Fig. 7(b) further examines the effect of spatial-grid mismatch. The continuous-location NF design and the fixed-grid NF codebook-based design achieve comparable performance for on-grid users. For randomly located off-grid users, their minimum user SEs are 0.02673 and 0.02131 bit/s/Hz, respectively, while the proposed WD design achieves 0.02643 bit/s/Hz. These results suggest that the advantage of the WD design over the fixed-grid codebook-based design primarily stems from its reduced sensitivity to spatial-grid quantization and off-grid mismatch. Low-wavenumber truncation mainly serves to reduce the number of retained modes and, consequently, the representation

dimension, with only a small performance loss under the evaluated conditions.

Table 3 compares the computational complexity and runtime of different beam design schemes. Here, C_c and C_f denote the coarse and fine NF codebook sets, respectively. Runtime is measured across 600 independent Monte Carlo realizations under identical simulation settings and reported as the mean ± standard deviation.

Table 3. Computational complexity and average runtime of the beam-design schemes.

Scheme	Overall Computational Complexity	Average Runtime (s)
Proposed-WD multi-beam design	$\mathrm{O}\left(KN\log N + NK^2 + K^3 + I_{\mathrm{BCD}}NK\right)$	0.049705±0.007734
NF codebook BCD-MM benchmark	$\mathrm{O}\left(KN\left(C_c + C_f\right) + K^3 + I_{\mathrm{BCD}}NK\right)$	0.162565±0.010122
NF-based single-beam design	$\mathrm{O}\left(KN\left(C_c + C_f\right) + NK\right)$	0.114948±0.005200
FF-based single-beam design	$\mathrm{O}\left(KN^2 + NK\right)$	0.000607±0.000178
Random phase design	$\mathrm{O}\left(N\right)$	0.000066±0.000117

6. Conclusion

This paper proposes a WD projection-based NF multiuser multi-beam design for XL-RIS-aided systems. The cascaded NF channel function and the XL-RIS reflection coefficient function are orthogonally projected onto a two-dimensional Fourier wavenumber basis. Circular low-wavenumber truncation yields a finite-dimensional representation, and a theoretical upper bound on the resulting truncation error is derived. The problem of maximizing the minimum user SE under the constant-modulus constraint is addressed through a fairness-oriented target-gain matching surrogate problem, which is solved using the BCD-MM algorithm. Simulation results demonstrate that the proposed method outperforms the considered benchmarks in terms of mean minimum user SE, lower-tail outage performance, and empirical satisfaction probability, indicating improved statistical reliability. The ablation results further suggest that the performance gain primarily stems from the reduced sensitivity of the WD representation to angle–distance quantization and off-grid mismatch, while low-wavenumber truncation provides a controllable trade-off between computational complexity and communication reliability. Future work will extend the proposed framework to multipath and wideband channels, user mobility, imperfect channel and location information, and finite-resolution phase shifts. Adaptive XL-RIS reconfiguration under dynamic propagation conditions will also be investigated.

Appendix A： Proof of lemma 1

From (24) and (28), the truncation error is given by the summation over the discarded modes as

$$g_k - \hat{g}_k = \sum_{\boldsymbol{m}\notin\mathrm{M}} \tilde{h}_{k,\boldsymbol{m}} w_{\boldsymbol{m}}. \tag{58}$$

Applying the Cauchy–Schwarz inequality to (58) yields

$$\left|g_k - \hat{g}_k\right| \le \left(\sum_{\boldsymbol{m}\notin\mathrm{M}} \left|\tilde{h}_{k,\boldsymbol{m}}\right|^2\right)^{1/2} \left(\sum_{\boldsymbol{m}\notin\mathrm{M}} \left|w_{\boldsymbol{m}}\right|^2\right)^{1/2}. \tag{59}$$

By the conjugate-symmetry property in (18), the orthogonality in (20), and Parseval's identity in (24), the wavenumber-domain coefficients in (23) satisfy $\sum_{\boldsymbol{m}} \left|\tilde{h}_{k,\boldsymbol{m}}\right|^2 = E_k$. Therefore, from the definition of η_k in Lemma 1, the

first factor in (59) satisfies

$$\sum_{\boldsymbol{m}\notin\mathrm{M}}\left|\tilde{h}_{k,\boldsymbol{m}}\right|^2=\left(1-\eta_k\right)E_k. \tag{60}$$

Similarly, by (20), (21), and Parseval's identity, together with the constant-modulus constraint, we have $\sum_{\boldsymbol{m}}\left|w_{\boldsymbol{m}}\right|^2=A_{\mathrm{R}}$ .Hence,

$$\sum_{\boldsymbol{m}\notin\mathrm{M}}\left|w_{\boldsymbol{m}}\right|^2\le A_{\mathrm{R}}. \tag{61}$$

Substituting (60) and (61) into (59) yields

$$\left|g_k-\hat{g}_k\right|\le\sqrt{\left(1-\eta_k\right)E_k\eta_k}, \tag{62}$$

which completes the proof.

Description

Table 4. Mathematical notation used in this study.

Notation	Meaning
a / $\boldsymbol{a}$ / $\boldsymbol{A}$	Scalar/vector/matrix
K / S_{R} / M	Set
$(\square)^{\mathrm{T}}$	Transpose
$(\square)^{\mathrm{H}}$	Conjugate transpose
$(\square)^{*}$	Complex conjugate
$\|\square\|_2$	Euclidean norm
$\angle(\square)$	Phase of a complex number
$\mathrm{Re}\{\cdot\}$ $\mathrm{Re}\{\square\}$	Real part
$\square$	Hadamard product
$\mathbb{C}^{m\times n}$ $\square^{m\times n}$	Set of $m\times n$ complex matrices

Data availability

The original contributions presented in this study are included in the article. Further inquiries can be directed to the corresponding author.

Author contributions

D.X. developed the methodology, performed the theoretical derivations, implemented the algorithms, conducted the simulations, prepared the figures, and wrote the original manuscript. G.Y. supervised the research and reviewed and edited the manuscript. Both authors reviewed and approved the final manuscript.

Funding

This work was partly supported by the National Natural Science Foundation of China (Grant No: 62261056) and the Qinghai Minzu University Key Scientific Research Project in Science and Engineering (Grant No: 2024XJZD01).

Competing interests

The authors declare no competing interests.

References

[1] Liu, Y. et al. Near-field communications: A comprehensive survey. *IEEE Commun. Surv. Tutorials* **27**, 1687–1728 (2025).

[2] Mu, X., Xu, J., Liu, Y. & Hanzo, L. Reconfigurable intelligent surface-aided near-field communications for 6G: Opportunities and challenges. *IEEE Veh. Technol. Mag.* **19**, 65–74 (2024).

[3] Wei, X., Dai, L., Zhao, Y., Yu, G. & Duan, X. Codebook design and beam training for extremely large-scale RIS: Far-field or near-field? *China Commun.* **19**, 193–204 (2022).

[4] Lu, H. et al. A tutorial on near-field XL-MIMO communications toward 6G. *IEEE Commun. Surv. Tutorials* **26**, 2213–2257 (2024).

[5] Liu, Y., Xu, J., Wang, Z., Mu, X. & Hanzo, L. Near-field communications: What will be different? *IEEE Wireless Commun.* **32**, 262-270 (2025).

[6] Lv, S., Liu, Y., Xu, X., Nallanathan, A. & Swindlehurst, A. L. RIS-aided near-field MIMO communications: Codebook and beam training design. *IEEE Trans. Wireless Commun.* **23**, 12531–12546 (2024).

[7] Liu, W. et al. Low-overhead beam training scheme for extremely large-scale RIS in near field. *IEEE Trans. Commun.* **71**, 4924–4940 (2023).

[8] Zhang, Q. et al. Multi-resolution codebook design and multiuser interference management for discrete XL-RIS-aided near-field MIMO systems. *IEEE Trans. Wireless Commun.* **25**, 2826–2842 (2026).

[9] Shen, D., Dai, L., Su, X. & Suo, S. Multi-beam design for near-field extremely large-scale RIS-aided wireless communications. *IEEE Trans. Green Commun. Netw.* **7**, 1542–1553 (2023).

[10] Zheng, X., Cheng, W., Wang, J. & Zhang, W. Location-driven beamforming for RIS-assisted near-field communications. *IEEE Commun. Mag.* **63**, 44–50 (2025).

[11] Xu, J., Mu, X. & Liu, Y. Exploiting STAR-RISs in near-field communications. *IEEE Trans. Wireless Commun.* **23**, 2181–2196 (2024).

[12] Lee, J., Chung, H., Cho, Y., Kim, S. & Hong, S. Near-field channel estimation for XL-RIS assisted multi-user XL-MIMO systems: Hybrid beamforming architectures. *IEEE Trans. Commun.* **73**, 1560–1574 (2025).

[13] Zheng, P., Lyu, X., Wang, Y. & Gong, Y. Convolutional dictionary learning-based hybrid-field channel estimation for XL-RIS-aided massive MIMO systems. *IEEE Trans. Wireless Commun.* **24**, 9085–9098 (2025).

[14] Wang, J., Xiao, J., Zou, Y., Xie, W. & Liu, Y. Wideband beamforming for RIS assisted near-field communications. *IEEE Trans. Wireless Commun.* **23**, 16836–16851 (2024).

[15] Hu, S., Wang, H. & Ilter, M. C. Design of near-field beamforming for large intelligent surfaces. *IEEE Trans. Wireless Commun.* **23**, 762–774 (2024).

[16] Wu, Z. & Dai, L. Multiple access for near-field communications: SDMA or LDMA? *IEEE J. Sel. Areas Commun.* **41**, 1918–1935 (2023).

[17] Wang, Z., Mu, X. & Liu, Y. Beamfocusing optimization for near-field wideband multi-user communications. *IEEE Trans. Commun.* **73**, 555–572 (2025).

[18] Zhang, H. et al. Beam focusing for near-field multiuser MIMO communications. *IEEE Trans. Wireless Commun.* **21**, 7476–7490 (2022).

[19] Li, Y. et al. Near-field beamforming optimization for holographic XL-MIMO multiuser systems. *IEEE Trans. Commun.* **72**, 2309–2323 (2024).

[20] Pizzo, A., Sanguinetti, L. & Marzetta, T. L. Fourier plane-wave series expansion for holographic MIMO communications. *IEEE Trans. Wireless Commun.* **21**, 6890–6905 (2022).

[21] Chen, Y. et al. Unified far-field and near-field in holographic MIMO: A wavenumber-domain perspective. *IEEE Commun. Mag.* **63**, 30–36 (2025).

[22] Guo, Y., Chen, Y. & Wang, Y. Channel estimation for holographic MIMO: Wavenumber-domain sparsity-inspired approaches. *IEEE Wireless Commun. Lett.* **13**, 2305–2309 (2024).

[23] Zhang, Z. & Dai, L. Wavenumber-domain signal processing for holographic MIMO: Foundations, methods, and future directions. *IEEE Commun. Stand. Mag.* **10**, 127–133 (2026).

[24] Zhang, Z. & Dai, L. Pattern-division multiplexing for multi-user continuous-aperture MIMO. *IEEE J. Sel. Areas Commun.* **41**, 2350–2366 (2023).

[25] Wu, H., Chen, Y., Ming, Y. & Wang, Z. Two-timescale beamforming optimization for downlink multi-user holographic MIMO surfaces. *IEEE Trans. Veh. Technol.* **73**, 4476–4481 (2024).

[26] Liu, Y. et al. CAPA: Continuous-aperture arrays for revolutionizing 6G wireless communications. *IEEE Wireless Commun.* **32**, 38–45 (2025).

[27] Zhao, B., Ouyang, C., Zhang, X. & Liu, Y. Continuous-aperture array (CAPA)-based wireless communications: Capacity characterization. *IEEE Trans. Wireless Commun.* **24**, 10456–10473 (2025).

[28] Wang, Z., Ouyang, C. & Liu, Y. Beamforming optimization for continuous aperture array (CAPA)-based communications. *IEEE Trans. Wireless Commun.* **24**, 5099–5113 (2025).

[29] Wang, Z., Ouyang, C. & Liu, Y. Optimal beamforming for multi-user continuous aperture array (CAPA) systems. *IEEE Trans. Commun.* **73**, 9207–9221 (2025).

[30] Ouyang, C., Wang, Z., Zhang, X. & Liu, Y. Diversity and multiplexing for continuous-aperture array (CAPA)-based communications. *IEEE Trans. Wireless Commun.* **24**, 8662–8680 (2025).

[31] Zhang, Y. et al. Exploiting continuous-aperture arrays in integrated sensing and communication systems. *IEEE Trans. Wireless Commun.* **24**, 9539–9555 (2025).